RSC Advances

PAPER

View Article Online
View Journal | View Issue

Cite this: *RSC Adv.*, 2025, **15**, 32654

Frequency-stable green EMI shielding in polyaniline-ferrite nanocomposites *via* dielectric and magnetic tuning

K. S. Mary Linsa, [ab] Viji C.,[bc] Roshila K. Pavithran,[ad] R. Rohith,[e] Sreekanth J. Varma, [e] Subodh Ganesanpotti, [f] K. S. Sibi[f] and U. S. Sajeev *[ag]

The need for advanced electromagnetic interference (EMI) shielding materials with minimal secondary radiation has driven interest in absorption-dominated or green EMI shielding systems. This work explored the development of efficient and frequency-stabilized green EMI shielding material based on polyaniline (PANI) by *in situ* incorporation of cobalt nickel ferrite (CNF) nanoparticles into the polymer matrix. EMI shielding effectiveness (SE) was measured in the K-band (18–26.5 GHz), achieving a maximum value of 68.96 dB for PANI/CNF10. All composites investigated in this study surpassed the commercial SE threshold of 30 dB, with shielding primarily governed by absorption. Reduced skin depth and high green index (GI) approaching unity confirmed their efficient absorption behavior. Further, multi-scale attributes of the composites were correlated to each other as well as to their EMI shielding behavior. Complementary optical, structural, and morphological analyses confirmed successful CNF integration and interaction with the PANI matrix. Dielectric and magnetic studies revealed enhanced AC conductivity, non-Debye relaxation, and improved coercivity, attributed to the synergistic effect of CNF addition into the PANI matrix. These results position PANI/CNF composites as promising green EMI shielding materials for next-generation electronic applications.

Received 23rd June 2025
Accepted 28th August 2025

DOI: 10.1039/d5ra04475h

rsc.li/rsc-advances

1 Introduction

The rapid development of high-performance electromagnetic interference (EMI) shielding materials is a result of the growing concern over pollution due to electromagnetic (EM) radiation, a consequence of the fast advancement of wireless electronics and the pervasive integration of electronic devices into daily life.[1] According to classical Schelkunoff transmission theory, EMI shielding effectiveness (SE) is directly proportional to electrical conductivity.[2,3] Traditional shielding materials such as metals, despite their high conductivity, suffer from limitations including high density, susceptibility to corrosion, poor flexibility, high cost, and difficulty in processing. As an alternative, conducting polymer (CP)-based nanocomposites have emerged as lightweight, corrosion-resistant, cheap, easily processable and tunable solutions for advanced EMI shielding applications.[4,5] The tunable electrical conductivity of CPs significantly aids the microwave absorption and EMI shielding capabilities of CP-based composites.[4]

An absorption-dominated shielding material, often referred to as a "green" shielding material, is characterized by an EMI shielding effectiveness (SE) exceeding 20 dB while maintaining EM wave reflections below 50%.[6] To achieve optimal performance, such materials must exhibit ideal impedance matching to minimize surface EM reflection, along with enhanced EM wave attenuation to maximize the overall shielding efficiency.[7–9] Intrinsically conducting polymers (ICPs) have become one of the most sought-after components in green EMI shielding due to their desirable absorption-dominant shielding mechanism.[10] By optimizing their composition and incorporating functional fillers, they enable the development of low-reflection, shielding materials, making them highly suitable for next-generation electronic devices operating in complex EM environments.[11] CP composites incorporated with magnetic fillers exhibit tunable EMI shielding performance, enabling effective EM wave absorption through dielectric loss and magnetic hysteresis loss. This unique characteristic offers the potential for developing green shielding materials with low reflection properties,

[a]*Post Graduate and Research Department of Physics, Government College Kottayam, Nattakom, Kerala 686013, India. E-mail: ussajeev@gmail.com*

[b]*Post Graduate and Research Department of Physics, Maharaja's College Ernakulam, Kochi, Kerala 682011, India*

[c]*Department of Physics, Government Polytechnic College, Palakkad, Kerala 678551, India*

[d]*Department of Physics, Sree Narayana Arts and Science College Kumarakom, Kottayam 686563, Kerala, India*

[e]*Materials for Energy Storage and Optoelectronic Devices Group, Department of Physics, Sanatana Dharma College, University of Kerala, Alappuzha, Kerala 688003, India*

[f]*Department of Physics, University of Kerala, Kariavattom Campus, Thiruvananthapuram 695581, India*

[g]*Department of Physics, Rajiv Gandhi Institute of Technology, Kottayam 686501, India*

making them suitable for applications requiring minimal secondary radiation.[10]

Among CPs, polyaniline (PANI) has gained considerable attention due to its tunable electrical conductivity,[12–15] environmental stability,[16] economic feasibility[17] and ease of synthesis through chemical oxidative polymerization.[18] These properties can be further tuned with the addition of various kinds of fillers that suit different applications. To enhance its EMI shielding properties, PANI can be hybridized with functional nanomaterials that provide synergistic improvements in electrical and magnetic properties.[19,20]

Introduction of magnetic nanofillers, particularly ferrites, offer a promising route to optimizing the shielding performance of PANI-based composites. The magnetic losses for radiations caused by eddy current effects, natural resonances, and anisotropy energy are increased by high permeability materials such as ferrites.[21,22] PANI/ferrite nanocomposites have intriguing hybrid properties that result from the collaborative blend of inorganic and organic constituents. Spinel-type ferrite nanoparticles, MFe_2O_4 (M = Ni, Co, Zn, Mn, Mg, *etc.*), have garnered great interest owing to their good EM performance. Cobalt ferrite, characterized by its mixed spinel structure, exhibits high coercivity and relatively low electrical resistivity. Nickel substitution into cobalt ferrites provides tunability of the magnetic and electrical attributes of ferrites as per the desired application.[23] Cobalt nickel ferrite (CNF) exhibits high saturation magnetization, excellent dielectric properties, and strong magnetic permeability, which are essential for improving the contribution of absorption towards EMI shielding.[24,25] The synergistic combination of high electrical conductivity of PANI and magnetic properties of CNF enables enhanced impedance matching, ensuring efficient dissipation of EM waves *via* conduction and magnetic loss mechanisms respectively. Furthermore, adjusting the CNF content in PANI can effectively tailor the shielding characteristics, balancing reflection, and absorption contributions to achieve a maximum and steady EMI shielding efficiency.[26–28]

In the existing literature, several PANI-based composites have been explored for EMI shielding. Carbon-loaded systems such as PANI/graphene[29] and PANI/CNTs[30] showed moderate SE values above 20 dB due to improved conductivity and polarization effects. Ferrite-based PANI hybrids[31,32] reached SE values above the industrial benchmark of 30 dB by combining dielectric and magnetic losses. Other PANI hybrids with MXenes[33] or oxides[34] have also been reported, though many still show higher reflection or limited frequency stability. While these studies exceeded the 30 dB requirement for practical use, little focus has been given to absorption-dominant or green shielding or the green index (GI). This gap forms the basis of the present work on PANI/CNF nanocomposites, designed for stable and eco-friendly shielding.

In this study, PANI/CNF nanocomposites were synthesized *via* simple and cost-effective *in situ* chemical oxidative polymerization method with varying weight fractions of CNF (5%, 10%, and 20%). The scattering parameters and SE indicating the microwave absorbing properties of the samples were measured in the technologically significant K-band frequency region (18–26.5 GHz). The optical, structural, and morphological characterization of the samples were performed through the characterization techniques *viz.* Ultraviolet-Visible (UV-Vis) absorption spectroscopy, Fourier Transform Infrared (FTIR) spectroscopy, X-ray Diffraction (XRD), Field Emission Scanning Electron Microscopy (FESEM), and Energy-Dispersive X-ray (EDX) spectroscopy. Dielectric properties of the composites were studied and AC conductivity was measured as function of frequency and composition. Magnetic characterization further explored the impact of CNF integration on the magnetic response of the composites, providing insights into their suitability for EM applications. This investigation aided in developing cost-effective, efficient, and frequency-stabilized green EMI shielding materials having primary contribution of absorption losses leading to excellent EMI SE with high attenuation of EM waves. The composites showed stable shielding across the K-band with a GI value near unity, highlighting both performance and sustainability. In addition to evaluating the EMI shielding performance, this study also attempts to establish meaningful correlations among optical, structural, morphological, dielectric, and magnetic characteristics of the PANI/CNF composites, aiming to understand how these multiscale properties synergistically influence the shielding behaviour. The findings of this work underscore the importance of synergistic interactions between conducting and magnetic components in designing next-generation polymer-based shielding materials for aerospace, telecommunications, and flexible electronics applications.

2 Materials and method

Sol–gel method was employed to synthesis CNF nanoparticles[35,36] employing the raw materials Iron(III) nitrate nonahydrate ($Fe(NO_3)_3 \cdot 9H_2O$) (purity 98%), nickel(II) nitrate hexahydrate ($Ni(NO_3)_2 \cdot 6H_2O$) (purity 98%), cobalt(II) nitrate hexahydrate ($Co(NO_3)_2 \cdot 6H_2O$) (purity 99%) and ethylene glycol ($(CH_2OH)_2$) (purity 99.8%). PANI was prepared through the chemical oxidative polymerization of aniline monomers. Raw materials used were aniline [$C_6H_5NH_2$] (purity 99.5%), concentrated hydrochloric acid [HCl] (purity 37%), ammonium peroxodisulfate [$(NH_4)_2S_2O_8$] (purity 98%), chloroform [$CHCl_3$] (purity 99.8%), and acetone [CH_3COCH_3] (purity 99.5%). The details of synthesis are reported in our earlier work.[12] Further 5%, 10% and 20% of CNF were respectively added during the *in situ* oxidative polymerization of aniline, resulting in the formation of PANI/CNF5, PANI/CNF10 and PANI/CNF20 composites.[37] Deionized water was employed throughout in the process and all raw materials of AR grade purchased from Sigma-Aldrich Chemicals Private Ltd, India were used as received without further purification.

The EMI shielding effectiveness in the K-band region (18 GHz to 26.5 GHz) was calculated from the reflection (S_{11} and S_{22}) and transmission (S_{21} and S_{12}) scattering parameters measured using Vector Network Analyzer (VNA-Agilent E5071C) on cuboidal pellets (16 mm × 8 mm × 1.5 mm), employing the waveguide method. Dielectric studies in the frequency range of 100 Hz–2 MHz were done on pressed pellets (13 mm diameter)

at room temperature using an electrochemical workstation BioLogic SP200 (BioLogic, France). 7410S Vibrating Sample Magnetometer (VSM-Lake Shore Cryotronics, Inc., Ohio, US) was employed for the magnetic studies of the powder samples at room temperature. UV-Vis absorption spectra were documented using a 2600 UV-Vis Spectrophotometer [Shimadzu Corp., Japan] in the wavelength region 200 nm–800 nm. FTIR spectra were recorded on a NicoletTM iS50 FTIR Spectrometer [Thermo Fisher Scientific Inc., US] using the KBr pressed pellets technique for the range 4000–400 cm^{-1}. XRD patterns were obtained on an Aeris X-ray Diffractometer [Malvern Panalytical, UK] employing Cu-Kα radiation of wavelength 1.5406 Å. Morphological features and elemental composition of the samples were respectively studied using a a Zeiss Sigma FESEM instrument [Carl Zeiss AG, Germany] and a Jeol 6390LA/OXFORD XMX N SEM-EDX [Jeol USA Inc., US].

3 Results and discussion

3.1 Electromagnetic interference (EMI) shielding properties

In the present work, the effect of incorporation of magnetic CNF nanoparticles into PANI matrix was studied by evaluating the EMI shielding behaviour of PANI, CNF and PANI/CNF composites in K-band frequency region (18 GHz to 26.5 GHz). For this, 16 mm × 8 mm × 1.5 mm cuboidal pellets of PANI, CNF and PANI/CNF composites, which match the size of specific waveguide sample holder were made for VNA measurements and their shielding effectiveness (SE) were calculated using the S-parameters obtained (details of theory and calculation included in SI).

Fig. 1 shows the variation of shielding effectiveness due to reflection (SER), shielding effectiveness due to absorption (SEA) and total shielding effectiveness (SET) of CNF, PANI, PANI/CNF5, PANI/CNF10 and PANI/CNF20 composites. It can be inferred that PANI/CNF5, PANI/CNF10 and PANI/CNF20 composites have an efficient shielding effectiveness and microwave absorption characteristics when compared to pure PANI and pure CNF. In addition, the shielding is absorption dominated in PANI, PANI/CNF5, PANI/CNF10 as well as PANI/CNF20. The inclusion of CNF stabilised the EMI shielding performance of PANI over the entire K-band frequency region and has also enhanced the contribution of shielding effectiveness due to absorption (SEA) towards the total shielding effectiveness (SET), which is a sought-after characteristic of efficient shielding materials. Absorption-based shielding is preferred over reflection-based shielding, as reflected EM radiation can cause the shield to behave as a secondary emitter of EM waves.[38]

The EMI shielding parameters like average shielding effectiveness due to absorption (SEA_{av}), average shielding effectiveness due to reflection (SER_{av}), average shielding effectiveness (SET_{av}), maximum shielding effectiveness (SET_{max}), shielding effectiveness per thickness (SET/t), specific shielding effectiveness (SSE), absolute shielding effectiveness (ASE), percentage of shielding efficiency (SE in %), Skin depth δ and Green Index (GI) of all the samples are calculated and given in Table 1. PANI/CNF10 demonstrated superior EMI shielding performance relative to pristine PANI, marked by increased average absorption effectiveness (SEA_{av}), higher total shielding effectiveness (SET_{av}), and a reduced average reflection component (SER_{av}). These features underscore its suitability for frequency-

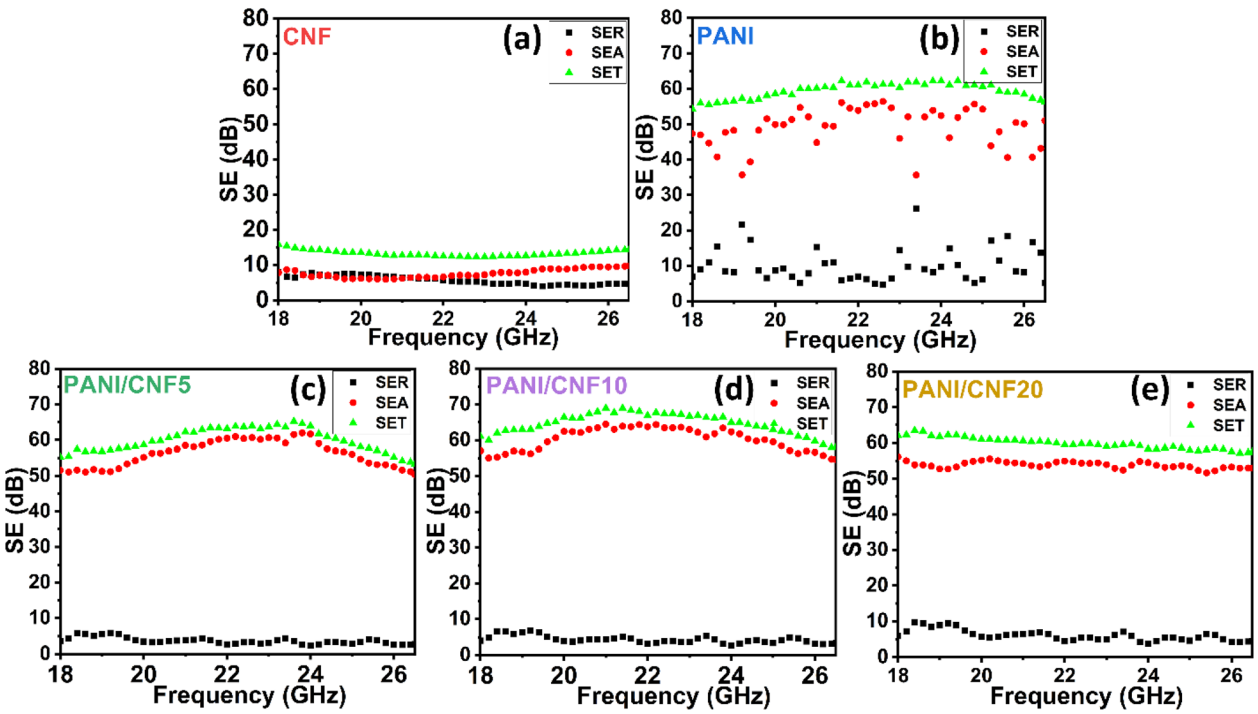

Fig. 1 SER, SEA and SET as a function of frequency of (a) CNF (b) PANI (c) PANI/CNF5 (d) PANI/CNF10 and (e) PANI/CNF20 in the K-band frequency region (18 GHz to 26.5 GHz).

Table 1 EMI shielding performance of CNF, PANI, PANI/CNF5, PANI/CNF10 and PANI/CNF20 composites

Sample	SEAav (dB)	SERav (dB)	SETav (dB)	SETmax (dB)	SET/t $\left(\frac{dB}{mm}\right)$	SSE $\left(dB\frac{cm^3}{g}\right)$	ASE $\left(dB\frac{cm^2}{g}\right)$	Shielding efficiency (%)	Skin depth δ (mm)	Green index (GI)
CNF	7.55	5.72	13.27	15.80	8.85	2.96	19.72	95.29022	1.768	0.699
PANI	49.58	9.95	59.54	63.09	39.69	42.99	286.66	99.99988	0.266	0.201
PANI/CNF5	56.3	3.73	60.03	65.23	40.02	49.26	328.43	99.99990	0.232	0.944
PANI/CNF10	**60.38**	**4.37**	**64.74**	**68.96**	**43.16**	**52.47**	**349.79**	**99.99996**	**0.216**	**0.818**
PANI/CNF20	53.85	6.09	59.94	63.48	39.96	41.63	277.55	99.99989	0.242	1.168

stabilized and green EMI shielding applications with minimal secondary radiation.

Fig. 2 shows the EMI shielding performance of CNF, PANI, PANI/CNF5, PANI/CNF10 and PANI/CNF20 composites expressed in terms of maximum shielding effectiveness (SET_{max}), average shielding effectiveness (SET_{av}), shielding effectiveness per thickness (SET/t), specific shielding effectiveness (SSE), absolute shielding effectiveness (ASE) and percentage of shielding efficiency (SE(%)). It can be inferred that though the shielding performance of pure CNF is poor when compared with pristine PANI, the shielding parameters of PANI improve with the incorporation of CNF in the composites PANI/CNF5 and PANI/CNF10. The synergistic combination of dielectric and magnetic properties in PANI/CNF composites plays a crucial role in their superior EMI shielding performance. According to Wang *et al.*, selectively assembling and expressing dielectric and magnetic "genes" yields a range of synergistic effects, including dipole polarisation, magnetic resonance, eddy currents, and charge transports that favour microwave-absorbing properties of materials.[39] The well-established conductive pathways within the composites facilitates strong Maxwell–Wagner interfacial polarization and promotes multiple internal reflections of incident EM waves.[40] This aids in the dissipation of EM energy through Joule heating and leakage currents. Additionally, the incorporation of magnetic CNF introduces abundant dipoles within the PANI matrix, leading to significant magnetic losses that further contribute to effective EM absorption.[41] These combined mechanisms effectively balance the dielectric and magnetic loss in PANI/CNF composites and thus establish them as highly efficient shielding materials, making them promising candidates for advanced EMI shielding applications.

Of all the samples, a maximum EMI SE of 68.96 dB which corresponds to 99.9999% shielding efficiency is obtained for PANI/CNF10. Adding to this, the composite has increased SEA and decreased SER when compared to pure PANI, which is a desirable trait for green EMI shielding. However, the incorporation of CNF into the PANI matrix beyond an optimal amount adversely affects its EM shielding performance. This can be attributed to possible filler agglomeration at higher concentrations, which may disrupt the continuity of conductive network and increase interfacial scattering, thereby impeding efficient charge mobility. Additionally, excessive magnetic filler can affect the impedance matching and thus saturate the microwave absorption capability. Hence, PANI/CNF10 marks the optimum balance between electrical conductivity, magnetic loss, and structural compatibility required for maximum EMI shielding in the K-band. Maximum EM wave absorption can be achieved when the values of dielectric loss and magnetic loss are closely matched thus minimizing impedance mismatch and enhancing energy dissipation through both dielectric polarization and magnetic resonance mechanisms.[42,43] The variation of skin depth of pure CNF, PANI and PANI/CNF composites, with K-band frequency is shown in Fig. 3(a). The average skin depth of the samples is given in Table 1. Among all samples studied, the value of δ is the lowest for PANI/CNF10 which makes it an efficient candidate for thin EMI shields.

Green shielding materials demand high absorption and low reflection towards incident EM wave.[44] This feature which assesses the eco-friendliness of shielding materials,[20] is

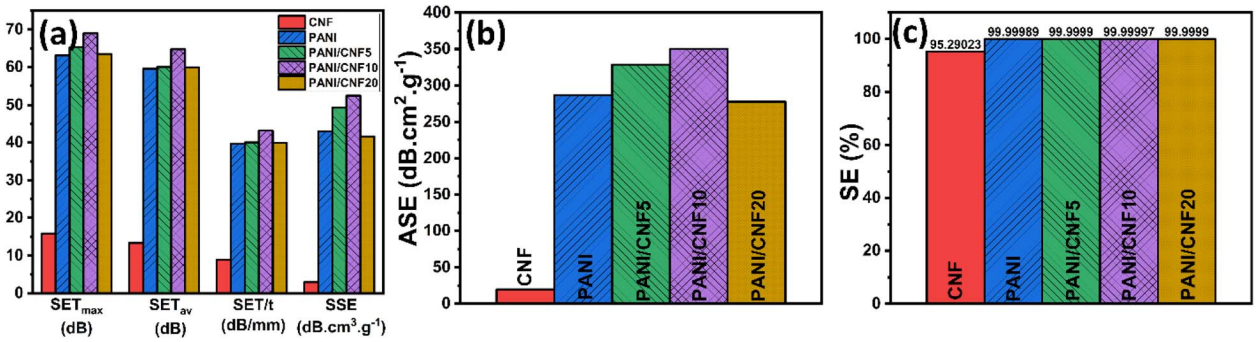

Fig. 2 Shielding performance of CNF, PANI, PANI/CNF5, PANI/CNF10 and PANI/CNF20 in the K-band frequency region (18 GHz to 26.5 GHz) in terms of (a) SE_{max}, SET_{av}, SET/t and SSE (b) ASE (c) SE (%).

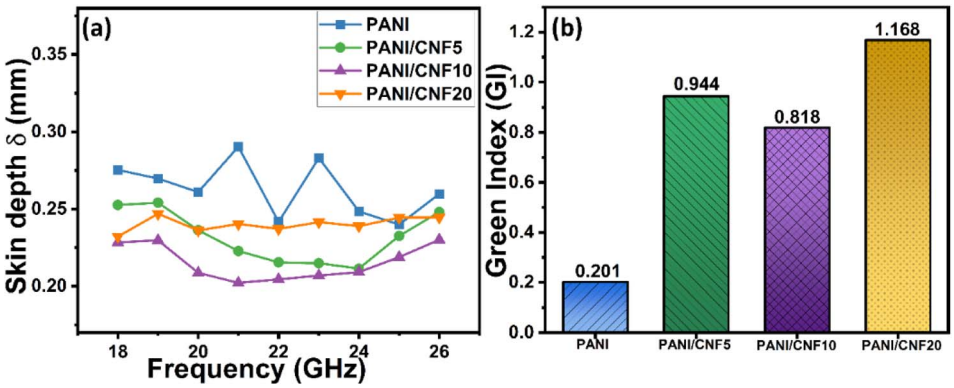

Fig. 3 Variation of (a) skin depth δ and (b) green index GI of PANI, PANI/CNF5, PANI/CNF10 and PANI/CNF20.

quantified by a factor termed green shielding index or green index (GI), first introduced by Cao *et al.*[45] GI evaluates the balance between absorption and reflection of incident EM waves and is given by the eqn (1).

$$\mathrm{GI} = \frac{\mathrm{SEA}}{\mathrm{SET}} = \frac{1}{|S_{11}{}^2|} - \frac{|S_{21}{}^2|}{|S_{11}{}^2|} - 1 \quad (1)$$

GI values close to unity indicate absorption-dominated shielding, minimizing secondary EM pollution, whereas lower values reflect reflection-dominated mechanisms.

The value of GI is evaluated for CNF, PANI and PANI/CNF and is listed in Table 1. Fig. 3(b) depicts its variation for PANI, PANI/CNF5, PANI/CNF10 and PANI/CNF20. GI value is greatly improved for the PANI/CNF composites when compared to pure PANI, implying a synergistic behaviour of the composites towards green EMI shielding, when compared to their individual counterparts. Also, the value of GI is approaching 1 in the case of PANI/CNF composites, which makes them suitable as green shielding materials in the K-band frequency region. The integration of CNF, possessing superior magnetic properties, into the conductive PANI matrix induces a synergistic enhancement in the EM characteristics of PANI, thereby significantly improving its EMI shielding performance. From Table 1, it can be inferred that though PANI and its composites with CNF exhibit almost closer values for SE, the advantage of PANI/CNF composite lies in the fact that its GI value very much outweighs the GI value of pure PANI. GI value of the composite (PANI/CNF10) exhibiting maximum SE, is about 4 times that of pure PANI. Adding to this, the SE value of the composites is almost stable over the entire frequency range when compared to the performance of pure PANI. The PANI/CNF composites with improved GI approaching the value of 1 and frequency-stabilized SE exceeding 30 dB indicates the higher performance and environment friendly EM shielding nature of the composites.[46]

3.2 Band gap (E_g) determination and Urbach tail analysis

The optical absorption spectra of powder samples of CNF, PANI and PANI/CNF composites in the range of 200 nm to 800 nm are given in Fig. S1. According to the Tauc relation given by eqn (2), where α represents the absorption coefficient, h is the Planck's constant (6.626×10^{-34} J.s), ν denotes the frequency of radiation, β is a constant known as the band tailing parameter, γ is an index that takes the values 1/2, 3/2, 2 and 3 depending on the nature of electronic transition ($\gamma = 1/2$ for direct band gap and $\gamma = 2$ for indirect band gap) and E_g is the band gap energy,[47,48] an extrapolation of the linear region of plot $(\alpha h\nu)^2$ *vs.* $h\nu$ gives the value of the direct optical band gap. This is depicted in Fig. 4(a). In Fig. 4(b), the linear region of plot $(\alpha h\nu)^{1/2}$ *vs.* $h\nu$ is extrapolated to obtain the value of the indirect optical band gap.

$$(\alpha h\nu)^{\frac{1}{\gamma}} = \beta(h\nu - E_g) \quad (2)$$

The measured band gaps are given in Table 2. As the amount of CNF increases, the direct as well as indirect band gap energy of the composites decreases. This result can be well correlated to the increase in conductivity detailed in Section 3.5.[12,49,50]

According to the Urbach formula[51] given in eqn (3), the absorption coefficient $\alpha(\nu)$ for non-crystalline materials has an exponential dependency on photon energy ($h\nu$) below the basic absorption edge.

$$\alpha(\nu) = \alpha_0 \exp\left(\frac{h\nu}{E_U}\right) \quad (3)$$

Here h is Planck's constant, ν is the frequency of radiation, α_0 is a constant and E_U is the Urbach energy. E_U is interpreted as the width of the tail of the localized states in the forbidden band gap and its emergence is attributed to thermal vibrations within the lattice structure.[52]

Plot of $(\ln \alpha)$ *vs.* energy for the determination of Urbach energy is displayed in Fig. 5. E_U is determined as the reciprocal of the slope of the linear component of these plots at lower energy values. The E_U values of PANI and PANI/CNF composites are determined and given in Table 2.

It is revealed that as the percentage of CNF in the PANI matrix rises, E_U value increases. It is observed that the band gap is inversely correlated with Urbach energy. As optical absorption spectra of all samples have been recorded at room temperature, the increase in Urbach tail width in the PANI matrix with CNF inclusion is thought to be solely caused by the increase in structural disorder,[53] which results in the development of defect

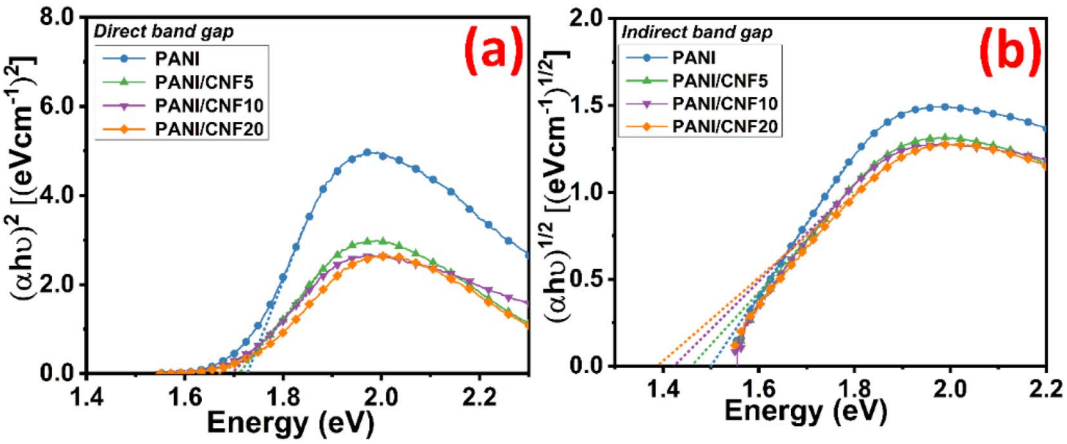

Fig. 4 Tauc plots depicting (a) direct band gap and (b) indirect band gap of CNF, PANI, PANI/CNF5, PANI/CNF10 and PANI/CNF20.

Table 2 Direct and indirect band gap energies of PANI and PANI/CNF composites

	Direct band gap energy	Indirect band gap energy	Urbach energy
Sample code	E_g in eV	E_g in eV	E_U in eV
PANI	1.724	1.505	0.118
PANI/CNF5	1.708	1.463	0.133
PANI/CNF10	1.695	1.424	0.149
PANI/CNF20	1.668	1.388	0.176

states inside the band tail.[54] This very well reasons the decrease in E_g and increase in E_U of PANI/CNF composites with increasing weight percentage of CNF. An increase in E_U with CNF incorporation indicates the presence of enhanced localized states and defect densities in PANI/CNF composites when compared to pure PANI. These defect states can facilitate defect-induced polarization, thereby increasing dielectric loss. Dielectric loss, being a key contributor to absorption of EM waves,[55] the observed rise in E_U indirectly supports the improved shielding performance of the PANI/CNF composites as discussed in Section 3.1.

3.3 Structural studies

The FTIR spectra of PANI/CNF composites, given in Fig. S2 confirmed the successful formation of composites during the *in situ* polymerization of aniline in the presence of varying amounts of CNF. All PANI/CNF composites exhibited spectra that carries most of the primary characteristic peaks of pure PANI. However, distinction of intensities of FTIR peaks can be associated to the variations in protonation or oxidation levels of PANI with the inclusion of varying amounts of CNF in it during the composite formation.[56,57]

The structural information and crystallinity extent of the prepared samples were established by XRD analysis. The XRD patterns of CNF, PANI, PANI/CNF5, PANI/CNF10 and PANI/CNF20 samples registered in the 2θ range from 20° to 80° are given in Fig. S3.

The degree of crystallinity is expressed in terms of crystallinity index (CI). It is determined from the ratio of the area of crystalline peak to the total peak area,[15] employing OriginPro software. The value of CI of CNF was found to be 33.90% and it was the maximum among all samples. CI value increased as the weight percentage of CNF in PANI/CNF composites increased, implying an increase in degree of crystallinity of PANI with the incorporation of CNF. As per the previous studies on PANI, conductivity of PANI has a significant dependence on the type of the dopant, the synthesis method[58] and the degree of crystallinity.[59] The increase in degree of crystallinity of PANI/CNF20 in comparison with that of pristine PANI can be associated to the improvement in conductivity of PANI with the incorporation of CNF.

The values of crystallinity index (CI), *d*-spacing (d) and interchain distance (R) of CNF, PANI, PANI/CNF5, PANI/CNF10 and PANI/CNF20 are summarized in Table 3. The CI value of PANI/CNF composites increased and values of d and R decreased as the weight fraction of CNF increased. This may be attributed to the modification in structural ordering and chain stacking that enhances the π–π interactions, further facilitating more efficient charge delocalization and interchain hopping. Consequently, the electrical conductivity of the composites improved with increasing CNF content (Section 3.5), indicating a strong correlation between microstructural ordering and charge transport properties.

3.4 Field emission scanning electron microscopy-energy dispersive X-ray analysis (FESEM-EDX)

In addition to the electrical and magnetic behaviour, EMI shielding performance of a material is dependent on its structural morphology as well.[60] FESEM images were recorded to estimate the particle size distribution in a better resolution. The FESEM images of PANI, CNF and PANI/CNF10 are given in Fig. 6. FESEM images reveal that particles of both PANI and PANI/CNF10 are of roughly spherical morphology and have an agglomeration tendency. When compared to pure PANI, PANI/CNF10 exhibited a more porous structure with notable reduction in aggregation of nanoparticles. A porous structure reduces

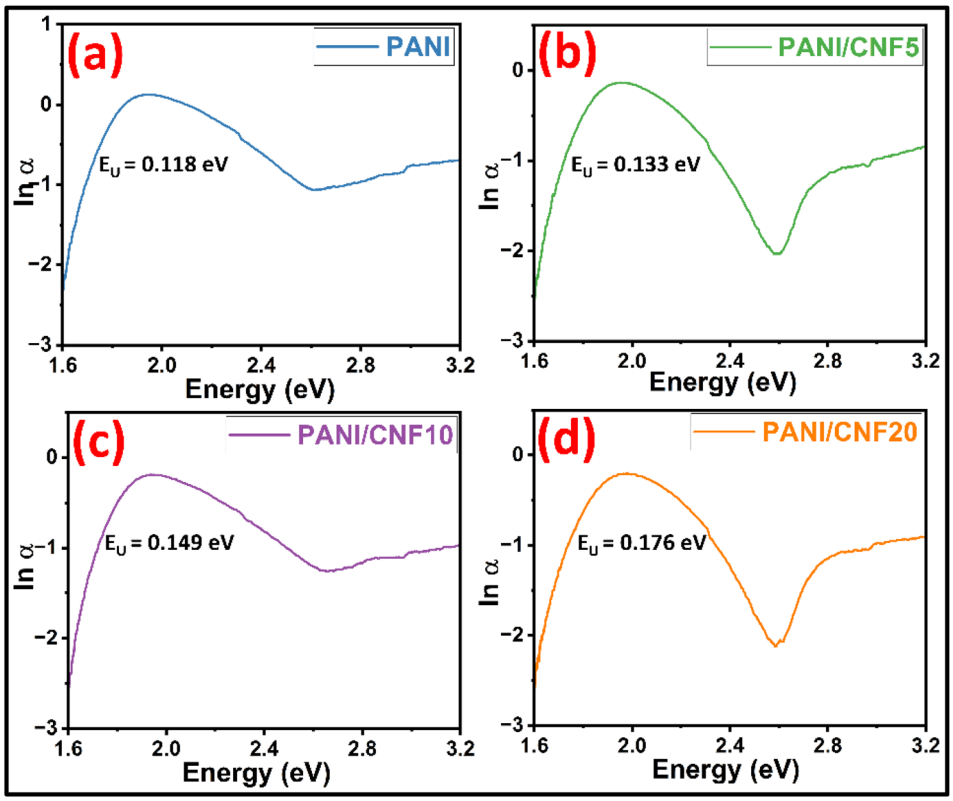

Fig. 5 Plot of (ln α) *vs.* energy of (a) PANI, (b) PANI/CNF5, (c) PANI/CNF10 and (d) PANI/CNF20.

Table 3 Crystallinity index, average *d*-spacing and average interchain separation of CNF, PANI and PANI/CNF composites

Sample name	Crystallinity index (CI) %	Average *d*-spacing (*d*) nm	Average interchain separation (*R*) nm
CNF	33.90	0.206	0.257
PANI	16.75	0.358	0.447
PANI/CNF5	23.07	0.336	0.419
PANI/CNF10	29.91	0.295	0.369
PANI/CNF20	31.02	0.265	0.332

material density, while increasing interfacial losses and extending the conduction path, thereby enhancing EM wave absorption.[9,61]

The particle size of the samples was determined from the FESEM images using ImageJ software. The distribution charts depicting the particle size of pure PANI, CNF and PANI/CNF10, are shown in Fig. 7. It is found that particle size of PANI/CNF10 composite (181 ± 44 nm) was larger when compared to pure CNF (120 ± 35 nm) and considerably smaller when compared to pure PANI (425 ± 84 nm). These findings imply that PANI has a tendency of forming a coating on the surface of CNF nanoparticles during the formation of PANI/CNF composite *via in situ* polymerization.[62]

The elemental composition of PANI, CNF and PANI/CNF20 samples as determined from the EDX is given in Table 4. The EDX analysis of PANI indicated the presence of carbon (C), oxygen (O), nitrogen (N), chlorine (Cl), and sulphur (S) in it. The occurrence of S and Cl in the synthesized PANI can be respectively attributed to the usage of APS as oxidizing agent and HCl as protonic acid during the synthesis of PANI. Presence of Fe, Co, Ni, and O elements are found in the CNF sample, as expected and this confirms the phase purity of the sample prepared. EDX spectra of PANI/CNF20 validates the successful incorporation of CNF into the PANI matrix. XRD analyses of the samples (Section 3.3) supports these results derived from EDX.

3.5 Dielectric studies

The dielectric parameters *viz.* impedance Z^*, permittivity K^*, and modulus M^* of CNF, PANI, PANI/CNF5, PANI/CNF10 and PANI/CNF20, defined by eqn (S16)–(S18) in SI, are depicted as a function of frequency in Fig. 8(a)-(f).

Fig. 8(a) depicts the variation of the real part of impedance (Z') with frequency for CNF (inset), PANI, and PANI/CNF composites. A general decrease in Z' with increasing frequency is observed, indicating enhanced electrical conduction across all samples. At low frequencies, Z' shows a sigmoid behavior that transitions into saturation at higher frequencies, suggesting the presence of mixed polarization mechanisms such as electronic, dipolar, and orientational polarization.[63] Among the composites, PANI/CNF20 exhibits the highest Z' at low frequencies and the lowest at high frequencies, likely due to improved grain connectivity facilitating charge transport.[64] Fig. 8(b) presents the imaginary part of impedance (Z'') as a function of frequency. All samples display a relaxation peak,

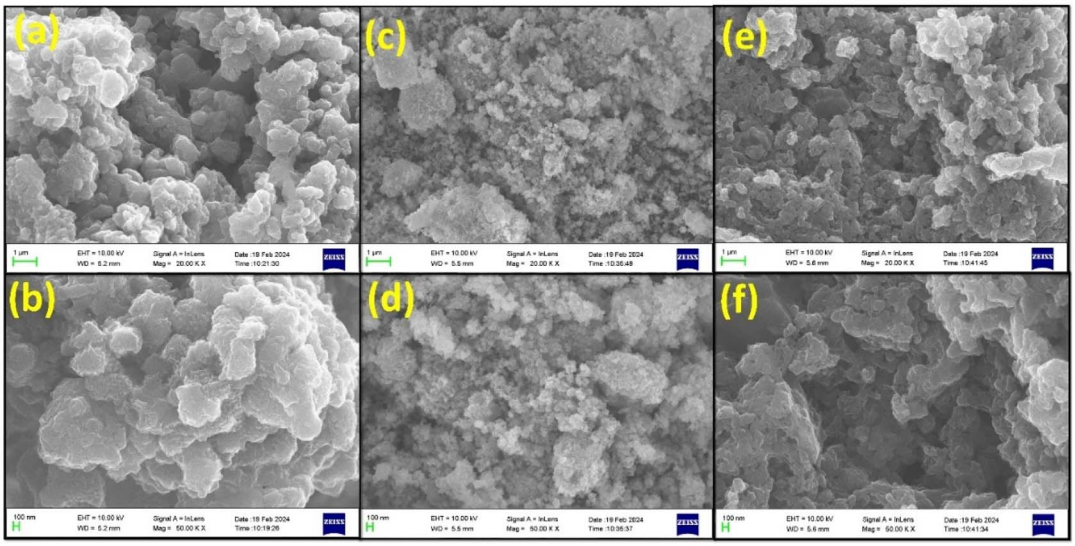

Fig. 6 FESEM images of (a and b) PANI, (c and d) CNF and (e and f) PANI/CNF10.

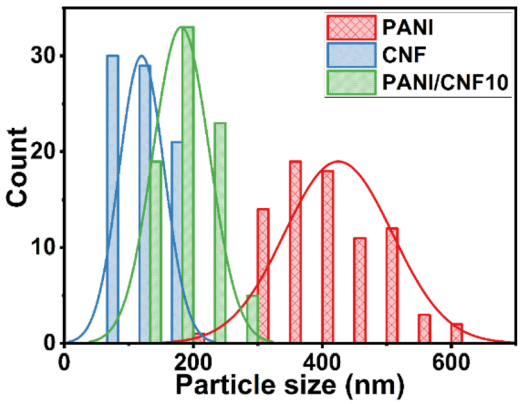

Fig. 7 Particle size distribution of CNF, PANI and PANI/CNF10.

which shifts toward lower frequencies and increases in magnitude with rising CNF content, indicating space charge relaxation effects becoming more prominent with CNF incorporation.[65,66]

As shown in Fig. 8(c) and (d), both the real (K') and imaginary (K'') parts of the dielectric constant decrease with increasing frequency and plateau at high frequencies due to dielectric relaxation.[67] This decline at lower frequencies is attributed to polarization effects, particularly space-charge and interfacial polarization.[68–71] In PANI/CNF composites, CNF nanoparticles act as dielectric barriers between conducting PANI chains, forming nanoscale capacitors that enhance dielectric permittivity. At high frequencies, the merging of all curves results from the loss of space-charge polarization, as dipoles can no longer follow the rapidly oscillating field.[72]

The complex electric modulus (M^*) provides insight into the bulk properties, conduction dynamics, electrode polarization, and relaxation behavior of the material. As shown in Fig. 8(e), the real part of complex modulus (M') approaches zero at low frequencies, indicating negligible electrode contribution.[73] With increasing frequency, M' rises and tends toward saturation, reflecting localized motion of charge carriers under an external field.[63,74,75] Fig. 8(f) displays the imaginary part (M''), which exhibits a single relaxation peak that shifts to higher frequencies and decreases in magnitude with increasing CNF content. This peak shift is attributed to microstructural changes and cation redistribution,[68] while the asymmetry of the peaks

Table 4 Elemental composition of PANI, CNF and PANI/CNF20

PANI				CNF				PANI/CNF20			
Element	Line type	wt %	Atomic %	Element	Line type	wt %	Atomic %	Element	Line type	wt %	Atomic %
C	K series	63.06	75.33	O	K series	27.72	57.7	C	K series	39.06	53.75
N	K series	3.27	3.35	Fe	K series	45.79	27.3	N	K series	8.54	10.08
O	K series	14.65	13.14	Co	K series	13.79	7.79	O	K series	23.8	24.59
S	K series	11.3	5.06	Ni	K series	12.71	7.21	S	K series	9.82	5.06
Cl	K series	7.72	3.12	—	—	—	—	Cl	K series	6.18	2.88
—	—	—	—	—	—	—	—	Fe	K series	6.96	2.06
—	—	—	—	—	—	—	—	Co	K series	2.76	0.77
—	—	—	—	—	—	—	—	Ni	K series	2.88	0.81
Total	—	100	100	Total	—	100	100	Total	—	100	100

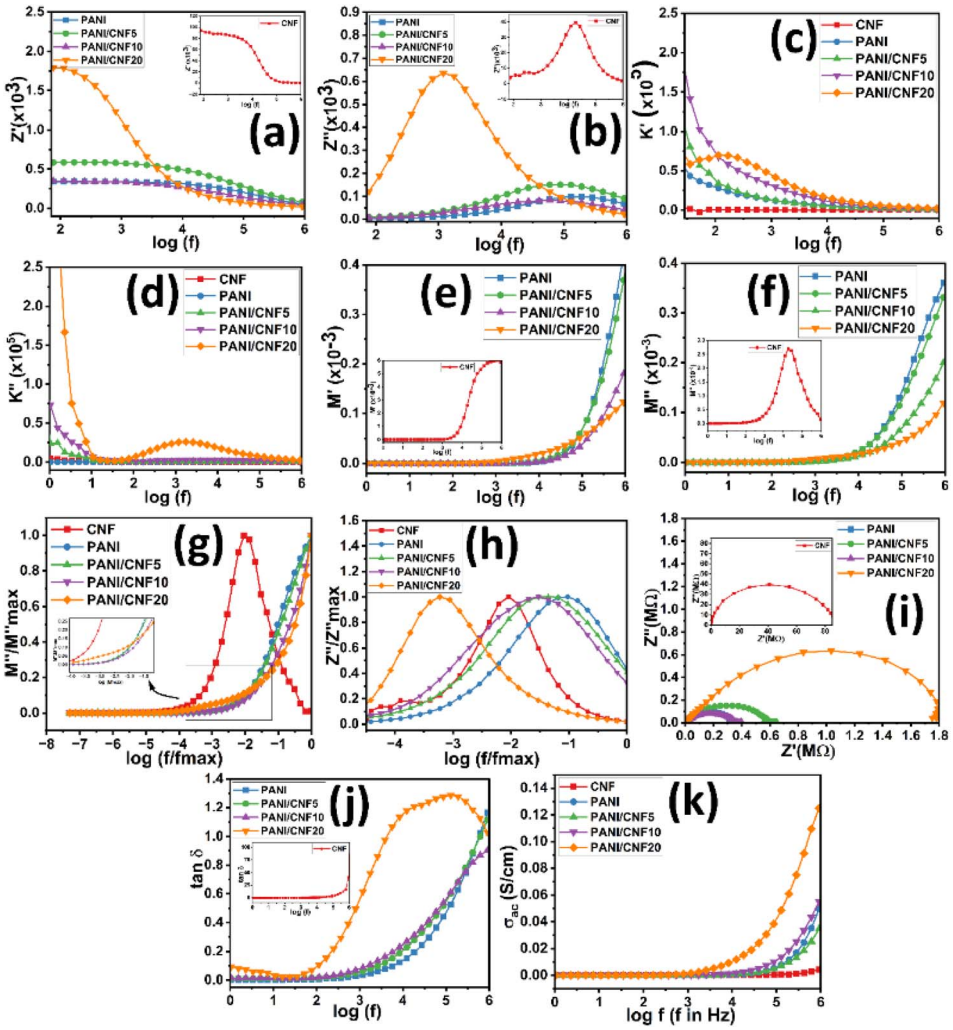

Fig. 8 (a) Real part of Z^* *vs.* log(f) (b) imaginary part of Z^* *vs.* log(f) (c) real part of K^* *vs.* log(f) (d) imaginary part of K^* *vs.* log(f) (e) real part of M^* *vs.* log(f) (f) imaginary part of M^* *vs.* log(f) (g) normalised modulus spectrum (M''/M''_{max}) *vs.* log(f/f_{max}) (h) normalised impedance spectrum (Z''/Z''_{max}) *vs.* log(f/f_{max}) (i) Nyquist plot (Z' *vs.* Z'') (j) loss tangent tan δ *vs.* log(f) and (k) σ_{ac} *vs.* log(f) of CNF, PANI, PANI/CNF5, PANI/CNF10 and PANI/CNF20 composites.

confirms the non-Debye relaxation behavior in all samples.[76] Fig. 8(g) and (h) show the normalised modulus spectrum [(M''/M''_{max}) *vs.* log(f/f_{max})] and normalised impedance spectrum [(Z''/Z''_{max}) *vs.* log(f/f_{max})] respectively. For all the samples, both showed a peak with a slight asymmetric broadening. Asymmetric peak broadening can be due to the occurrence of electrical processes in the material with a spread of relaxation time[77]

Fig. 8(i) shows the Nyquist plots (Z' *vs.* Z'') at room temperature. The distorted semicircles with centers below the real axis confirm non-Debye relaxation behavior.[67] A single dominant semicircle followed by a low-frequency tail indicates the combined influence of grains and grain boundaries, with grain effects being predominant in both PANI and PANI/CNF composites.[78]

The dielectric loss tangent (tan δ) of the material can be calculated using the eqn (4). The variation of tan δ as a function of the frequency of the samples is shown in Fig. 8(j).

$$\tan\ \delta = \frac{K''}{K'} \tag{4}$$

A peak in tan δ is observed at a characteristic frequency for all samples. The peak is slightly elevated and shifted towards the low frequency end in PANI/CNF20 when compared to pure PANI, PANI/CNF5 and PANI/CNF10 samples. This can be associated to enhanced relaxation time and elevated dielectric loss in PANI/CNF20 composite when compared to pure PANI and other PANI/CNF composites.

Fig. 8(k) presents the variation of AC conductivity (σ_{ac}) with log$f$ for all samples. The plots exhibit two distinct regions: a low-frequency plateau where conductivity is nearly constant, followed by a high-frequency region where σ_{ac} increases with frequency. This behavior, typical of disordered systems, indicates charge transport primarily *via* hopping mechanisms. The observed trend aligns with Jonscher's universal power law,[79]

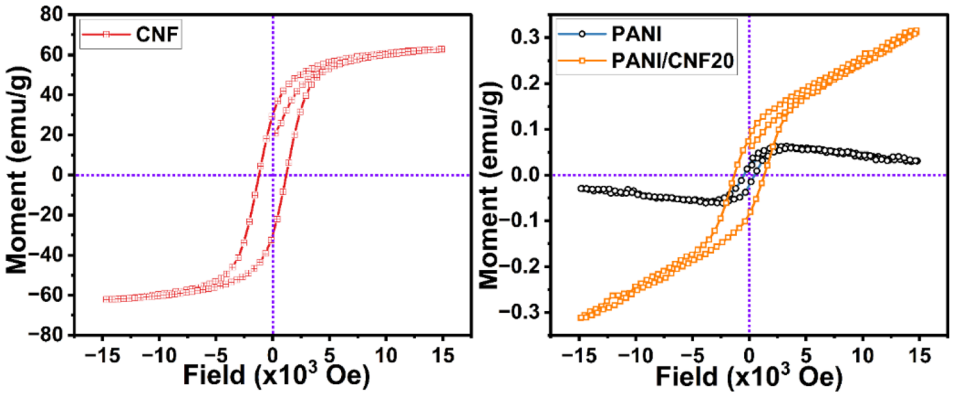

Fig. 9 M–H curves of CNF, PANI and PANI/CNF20 composites.

confirming that the AC conductivity in PANI and its CNF composites is governed by relaxation processes involving mobile charge carriers.[80,81] It can be inferred that the addition of CNF enhanced conductivity by promoting charge transfer within the PANI chain.[56] Consequently, judicious doping with varying weight fraction of CNF allows for the optimization of conductivity in PANI/CNF composites employable for EMI shielding applications.

The simultaneous increase in dielectric loss and AC conductivity with increasing CNF content in PANI/CNF nanocomposites can be attributed to enhanced interfacial polarization and improved charge carrier mobility. This facilitates effective energy dissipation and charge transport under alternating EM field thus contributing to superior absorption-dominated EMI shielding performance,[82] as observed in the optimized PANI/CNF composites (Section 3.1). To tailor the EM absorption performance, particularly in the gigahertz (GHz) range, it is necessary to fine-tune various factors affecting dielectric loss *viz.* atomic polarization, ionic polarization, dipole/molecular polarization, defect-induced polarization, and interfacial polarization.[83] Hence an optimum balance between the concentration of ferrites and polymer is important in accomplishing improved EM shielding applications.[84]

3.6 Magnetic studies

Fig. 9 shows M–H curves recorded at room temperature for CNF, PANI, and PANI/CNF20 samples. A clear hysteretic behavior is observed in all the samples. Table 5 gives the values of saturation magnetization (M_s), remanence magnetization (M_r) and coercivity (H_c) of the samples.

Table 5 Comparison of saturation magnetization (M_s), remanence magnetization (M_r) and coercivity (H_c) of PANI, CNF and PANI/CNF20 composite

Sample code	M_s (emu g^{-1})	M_r (emu g^{-1})	H_c (Oe)
PANI	0.062	0.023	467.280
CNF	62.400	29.900	1204.300
PANI/CNF20	0.314	0.083	1319.800

The CNF sample exhibits a typical ferrimagnetic nature of M–H curve. Its narrow S-shaped hysteresis loop is indicative of its soft magnetic nature, which is a characteristic of spinel ferrites. Ferrites that possess this magnetic flexibility, are reported to aid in EM-absorbing substances, dielectric resonators, and monolayer chip inductors.[85,86] The magnetic parameters of the CNF sample agree with the corresponding values reported by Sahare *et al.*[87] As reported by Shelar *et al.*[88] and Sahare *et al.*,[87] cobalt-doped nickel ferrite exhibits improved magnetic properties than nickel ferrite (NF). In this study, CNF doping into PANI has very well improved the magnetic properties of PANI.

Table 5 shows that the incorporation of CNF into PANI matrix has led to a considerable increase in coercivity (H_c), a factor that depends on inter-particle interactions and surface anisotropy. Particle size shows an inverse correlation, while porosity exhibits a direct correlation with coercivity.[89] The elevated H_c value of PANI/CNF when compared with that of pure PANI can be associated with its reduced particle size and enhanced porosity as inferred from FESEM studies detailed in Section 3.4. When compared to pure PANI, the M_s and M_r values show an increase in the nanocomposites, attributed to the presence of CNF. This improvement in magnetic properties of PANI upon incorporation of CNF is primarily due to the intrinsic magnetic behaviour of the ferrite phase, which imparts high magneto-crystalline anisotropy and stable domain structures.[90,91] This contributes significantly to improved EMI SE through magnetic hysteresis and resonance-related losses.[42,92] However, optimizing the size and concentration of magnetic nanoparticles within PANI matrix is crucial for achieving desirable magnetic properties suiting multifunctional material development based on ferrite/polymer nanocomposites.[93,94]

4 Conclusion

This study demonstrates the development of PANI/CNF nanocomposites as high-performance, frequency-stabilized green EMI shielding materials in the K-band frequency region. Among all the compositions studied, PANI/CNF10 emerged as the most effective absorption-dominant shielding material, as evidenced by its enhanced SEA_{av} and SET_{av} values along with a reduced SER_{av}, affirming its potential for green EMI shielding

applications with suppressed secondary radiation. PANI/CNF10 exhibited the highest EMI SE of 68.96 dB, far surpassing the industrial threshold of 30 dB required for commercial applications. The shielding mechanism was predominantly absorption-driven and consistent across the frequency range, reflecting effective dielectric and magnetic loss mechanisms. Furthermore, the reduction in skin depth and the green index approaching unity emphasize the dual advantage of performance and sustainability. Moreover, an attempt has been made to establish interrelationships among the structural, morphological, optical, dielectric, and magnetic parameters of the material, and to correlate these intrinsic properties with its EMI shielding efficiency. These findings underscore the synergistic role of CNF in tailoring the EM properties of PANI, making PANI/CNF nanocomposites highly promising candidates for next-generation EMI shielding solutions in advanced electronics, with a focus on environmental responsibility.

Author contributions

K. S. Mary Linsa: conceptualization, sample preparation, formal analysis, writing – original draft, writing – review & editing. Viji C.: sample preparation. Roshila K. Pavithran: formal analysis. Rohith R.: formal analysis. Sreekanth J. Varma: writing – review & editing. Subodh Ganesanpotti: writing – review & editing. K. S. Sibi: writing – review & editing. U. S. Sajeev: formal analysis, writing – review & editing, validation, supervision.

Conflicts of interest

There are no conflicts to declare.

Data availability

Data are available upon request from the authors. Supplementary information (SI) is available. See DOI: **https://doi.org/10.1039/d5ra04475h**.

Acknowledgements

This work was supported by the Department of Science and Technology(DST), Government of India under a FIST 0-Level grant [SR/FST/COLLEGE-206/2014]; by the University grants Commission (UGC) under a Major Research Project (F no. 42.895/2012 (SR)); and by the Government of Kerala under the Center of Excellence (CoE) Project [A3-1307/2018/Plan 18–19]. The authors acknowledge the XRD Facility, St. Thomas College (Autonomous), Thrissur for structural studies; DST-SAIF, Sophisticated Test and Instrumentation Centre (STIC) and DST-FIST, Department of Physics, Cochin University of Science & Technology Campus(CUSAT) for optical and morphological studies; the Materials for Energy Storage and Optoelectronic Devices Group, Department of Physics, Sanatana Dharma College, Alappuzha for dielectric and conductivity studies; and VSM Lab, SAIF, IIT Madras for the magnetic studies. The authors acknowledge KSCSTE, Government of Kerala, and the DST, Government of India, for the instrumentation facilities provided under the SARD (No. 612/2016/KSCSTE) and FIST schemes (SR/FIST/College-227/2014(c) & SR/FST/COLLEGE-/2023/1454 (G)), respectively. The authors would like to acknowledge the Vector Network Analyzer facility at Microwave Materials Laboratory, Department of Physics, University of Kerala for the EMI shielding effectiveness measurement. During the preparation of this work, the authors used Chatgpt and Quillbot to improve the language and readability. After using these tools, the authors reviewed and edited the content as needed and takes full responsibility for the content of the publication.

References

1 S. Zheng, Y. Wang, X. Wang and H. Lu, *Mater. Today Phys.*, 2024, **40**, 101330.
2 X. Wu, T. Tu, Y. Dai, P. Tang, Y. Zhang, Z. Deng, L. Li, H.-B. Zhang and Z.-Z. Yu, *Nanomicro. Lett.*, 2021, **13**, 148.
3 Y. Zhang, K. Ruan and J. Gu, *Small*, 2021, **17**, 2101951.
4 P. Modak, S. B. Kondawar and D. V. Nandanwar, *Procedia Mater. Sci.*, 2015, **10**, 588–594.
5 P. Zarrintaj, H. Vahabi, M. R. Saeb and M. Mozafari, in *Fundamentals and Emerging Applications of Polyaniline*, Elsevier, 2019, pp. 259–272.
6 Z. Jia, C. Wang, A. Feng, P. Shi, C. Zhang, X. Liu, K. Wang and G. Wu, *Composites, Part B*, 2020, **183**, 107690.
7 Z. Cheng, R. Wang, Y. Wang, Y. Cao, Y. Shen, Y. Huang and Y. Chen, *Carbon*, 2023, **205**, 112–137.
8 X. Jia, Y. Li, B. Shen and W. Zheng, *Composites, Part B*, 2022, **233**, 109652.
9 M. Ma, X. Liang, W. Tao, Q. Peng, W. Shao, S. Chen, Y. Shi, H. He, Y. Zhu and X. Wang, *Compos. Struct.*, 2024, **342**, 118259.
10 Y. Yang, J. Li, Z. Wang, X. Ju, H. Duan and Y. Tang, *Adv. Nanocompos.*, 2024, **1**, 290–303.
11 X. Zhong, M. He, C. Zhang, Y. Guo, J. Hu and J. Gu, *Adv. Funct. Mater.*, 2024, **34**(19), DOI: **10.1002/adfm.202313544**.
12 K. S. Mary Linsa, R. K. Pavithran, R. J. Mathew, P. Radhakrishnan, R. Pragash and U. S. Sajeev, *J. Macromol. Sci. B*, 2024, **63**, 1–19.
13 Y. Long, Z. Chen, J. L. Duvail, Z. Zhang and M. Wan, *Phys. Rev. B:Condens. Matter Mater. Phys.*, 2005, **370**, 121–130.
14 J. Stejskal, A. Riede, D. Hlavatá, J. Prokeš, M. Helmstedt and P. Holler, *Synth. Met.*, 1998, **96**, 55–61.
15 S. Bhadra, N. K. Singha, S. Chattopadhyay and D. Khastgir, *J. Polym. Sci., Part B:Polym. Phys.*, 2007, **45**, 2046–2059.
16 N. Sharma, A. Singh, N. Kumar, A. Tiwari, M. Lal and S. Arya, *J. Mater. Sci.*, 2024, **59**, 6206–6244.
17 D. Ghosh, S. Giri, S. Kalra and C. K. Das, *Open J. Appl. Sci.*, 2012, **02**, 70–77.
18 K. Bednarczyk, W. Matysiak, T. Tański, H. Janeczek, E. Schab-Balcerzak and M. Libera, *Sci. Rep.*, 2021, **11**, 7487.
19 A. Rayar, C. S. Naveen, H. S. Onkarappa, V. S. Betageri and G. D. Prasanna, *Synth. Met.*, 2023, **295**, 117338.
20 S. Kumari, J. Dalal, A. Kumar, R. Pal, R. Chahal and A. Ohlan, *RSC Adv.*, 2024, **14**, 662–676.

21 A. P. Singh, M. Mishra, A. Chandra and S. K. Dhawan, *Nanotechnology*, 2011, **22**, 465701.
22 A. L. Kozlovskiy, I. E. Kenzhina and M. V. Zdorovets, *Ceram. Int.*, 2020, **46**, 10262–10269.
23 U. B. Sontu, V. Yelasani and V. R. R. Musugu, *J. Magn. Magn. Mater.*, 2015, **374**, 376–380.
24 I. S. Kapte, S. Niyogi, P. J. Qureshi, V. Khade, T. Avanish Babu, K. V. Siva kumar and W. Madhuri, *Ceram. Int.*, 2024, **50**, 30754–30762.
25 V. Shukla, *Nanoscale Adv.*, 2019, **1**, 1640–1671.
26 L. Abbasi, K. Hedayati and D. Ghanbari, *J. Mater. Sci.:Mater. Electron.*, 2021, **32**, 14477–14493.
27 S. P. Gairola, V. Verma, L. Kumar, M. A. Dar, S. Annapoorni and R. K. Kotnala, *Synth. Met.*, 2010, **160**, 2315–2318.
28 S. Chaturvedi, R. Das, P. Poddar and S. Kulkarni, *RSC Adv.*, 2015, **5**, 23563–23568.
29 Y. Chen, Y. Li, M. Yip and N. Tai, *Compos. Sci. Technol.*, 2013, **80**, 80–86.
30 L. Zou, C. Lan, L. Yang, Z. Xu, C. Chu, Y. Liu and Y. Qiu, *Diam. Relat. Mater.*, 2020, **104**, 107757.
31 R. T. Ma, H. T. Zhao and G. Zhang, *Mater. Res. Bull.*, 2010, **45**, 1064–1068.
32 S. Kumar, A. Ohlan, P. Kumar and V. Verma, *J. Supercond. Novel Magn.*, 2020, **33**, 1187–1198.
33 M. Liaquat, A. Arshad, F. A. Tahir, N. Shoaib and S. Rahman, *Results Eng.*, 2025, **25**, 103542.
34 M. Emek, E. İ. Şahin and J.-E. F. M. Ibrahim, *Appl. Sci.*, 2025, **15**, 3689.
35 F. Majid, J. Rauf, S. Ata, I. Bibi, A. Malik, S. M. Ibrahim, A. Ali and M. Iqbal, *Mater. Chem. Phys.*, 2021, **258**, 123888.
36 P. Lavela and J. L. Tirado, *J. Power Sources*, 2007, **172**, 379–387.
37 Swati, M. Saini, Anupama, R. Shukla, Vikram and P. Chand, *J. Inorg. Organomet. Polym. Mater.*, 2023, **33**, 1955–1968.
38 S. Kumari, J. Dalal, V. Kumar, A. Kumar and A. Ohlan, *Int. J. Mol. Sci.*, 2023, **24**, 12267.
39 X.-X. Wang, Q. Zheng, Y.-J. Zheng and M.-S. Cao, *Carbon*, 2023, **206**, 124–141.
40 R. Kumar, H. K. Choudhary, S. P. Pawar, S. Bose and B. Sahoo, *Phys. Chem. Chem. Phys.*, 2017, **19**, 23268–23279.
41 S. Kumar, P. Kumar, R. Gupta and V. Verma, *J. Alloys Compd.*, 2021, **862**, 158331.
42 K. A. Darwish, O. M. Hemeda, M. I. Abdel Ati, A. S. Abd El-Hameed, D. Zhou, M. A. Darwish and M. M. Salem, *Appl. Phys. A: Mater. Sci. Process.*, 2023, **129**, 460.
43 A. Motamedi, R. Rahmanifard and M. Adibi, *Synth. Met.*, 2021, **280**, 116873.
44 D. Q. Zhang, T. T. Liu, J. C. Shu, S. Liang, X. X. Wang, J. Y. Cheng, H. Wang and M. S. Cao, *ACS Appl. Mater. Interfaces*, 2019, **11**, 26807–26816.
45 X. X. Wang, J. C. Shu, W. Q. Cao, M. Zhang, J. Yuan and M. S. Cao, *Chem. Eng. J.*, 2019, **369**, 1068–1077.
46 J. Cheng, C. Li, Y. Xiong, H. Zhang, H. Raza, S. Ullah, J. Wu, G. Zheng, Q. Cao, D. Zhang, Q. Zheng and R. Che, *Nano-Micro Lett.*, 2022, **14**, 80.
47 P. Makuła, M. Pacia and W. Macyk, *J. Phys. Chem. Lett.*, 2018, **9**, 6814–6817.
48 A. S. Hassanien and A. A. Akl, *J. Alloys Compd.*, 2015, **648**, 280–290.
49 M. J. Almasi, T. Fanaei Sheikholeslami and M. R. Naghdi, *Composites, Part B*, 2016, **96**, 63–68.
50 S. Bhadra, D. Khastgir, N. K. Singha and J. H. Lee, *Prog. Polym. Sci.*, 2009, **34**, 783–810.
51 F. Urbach, *Phys. Rev.*, 1953, **92**, 1324.
52 M. D. Migahed and H. M. Zidan, *Curr. Appl. Phys.*, 2006, **6**, 91–96.
53 S. Banerjee and A. Kumar, *Nucl. Instrum. Methods Phys. Res., Sect. B*, 2011, **269**, 2798–2806.
54 J. John, S. Sivaraman and S. Jaylekshmi, *e-Polymers*, 2010, **10**, DOI: 10.1515/epoly.2010.10.1.87.
55 M. Qin, L. Zhang, X. Zhao and H. Wu, *Adv. Sci.*, 2021, **8**, 2004640.
56 P. Kolhar, B. Sannakki, M. Verma, S. Suresha, M. Alshehri and N. A. Shah, *Nanomaterials*, 2023, **13**, 2234.
57 R. Patil, A. S. Roy, K. R. Anilkumar, K. M. Jadhav and S. Ekhelikar, *Composites, Part B*, 2012, **43**, 3406–3411.
58 W. Łużny and E. Bańka, *Macromolecules*, 2000, **33**, 425–429.
59 R. P. McCall, J. M. Ginder, M. G. Roe, G. E. Asturias, E. M. Scherr, A. G. MacDiarmid and A. J. Epstein, *Phys. Rev. B*, 1989, **39**, 10174–10178.
60 Y. Zhang, J. Lu, J. Yu, W. Wang, S. Zhai, Y. Yu and D. Qi, *Composites, Part A*, 2025, **192**, 108764.
61 Q. Peng, M. Ma, Q. Chu, H. Lin, W. Tao, W. Shao, S. Chen, Y. Shi, H. He and X. Wang, *J. Mater. Chem. A*, 2023, **11**, 10857–10866.
62 J. Guo, Z. Chen, W. Abdul, J. Kong, M. A. Khan, D. P. Young, J. Zhu and Z. Guo, *Adv. Compos. Hybrid Mater.*, 2021, **4**, 534–542.
63 P. Kumari, R. Rai and A. L. Kholkin, *J. Alloys Compd.*, 2015, **637**, 203–212.
64 T. Rajyalakshmi, A. Pasha, S. Khasim, M. Lakshmi and M. Imran, *SN Appl. Sci.*, 2020, **2**, 530.
65 A. Kyritsis, P. Pissis and J. Grammatikakis, *J. Polym. Sci., Part B:Polym. Phys.*, 1995, **33**, 1737–1750.
66 J. PCHARSKI, *Solid State Ionics*, 1988, **28–30**, 979–982.
67 P. Jisha, M. S. Suma, M. V. Murugendrappa and K. Raj, *Int. J. Polym. Anal. Charact.*, 2020, **25**, 176–187.
68 W. E. Morton and J. W. S. Hearle, in *Physical Properties of Textile Fibres*, Elsevier, 2008, pp. 625–642.
69 M. G. Han and S. S. Im, *J. Appl. Polym. Sci.*, 2001, **82**, 2760–2769.
70 S. Saravanan, C. Joseph Mathai, M. R. Anantharaman, S. Venkatachalam and P. V. Prabhakaran, *J. Phys. Chem. Solids*, 2006, **67**, 1496–1501.
71 A. K. Pradhan, T. K. Nath and S. Saha, *Mater. Res. Express*, 2017, **4**, 076107.
72 X. W. Wang, Q. Q. Zhu, X. E. Wang, H. C. Zhang, J. J. Zhang and L. F. Wang, *J. Alloys Compd.*, 2016, **675**, 195–200.
73 V. Manju, R. Rohith, A. Thejas Prasannakumar, B. V. Bhavija and S. J. Varma, *New J. Chem.*, 2022, **46**, 19874–19887.
74 S. C. Panigrahi, P. R. Das, B. N. Parida, R. Padhee and R. N. P. Choudhary, *J. Alloys Compd.*, 2014, **604**, 73–82.
75 A. Sinha and A. Dutta, *RSC Adv.*, 2015, **5**, 100330–100338.

76 R. Brahem, Z. Raddaoui and M. Bourguiba, *J. Mater. Sci.: Mater. Electron.*, 2022, **33**, 4156–4169.
77 C. K. Suman, K. Prasad and R. N. P. Choudhary, *J. Mater. Sci.*, 2006, **41**, 369–375.
78 R. Verma, S. P. Tiwari, R. Kumari and R. Srivastava, *J. Mater. Sci.*, 2018, **53**, 4199–4208.
79 A. K. Jonscher, *Thin Solid Films*, 1978, **50**, 187–204.
80 A. Asha, S. L. Goyal, R. Dhankhar, R. Sharma and A. Sharma, *Indian J. Pure Appl. Phys.*, 2022, **60**, 982–988.
81 R. Moučka, N. Kazantseva and I. Sapurina, *J. Mater. Sci.*, 2018, **53**, 1995–2004.
82 J. Prasad, Y.-W. Choi, M. G. Nam, M.-W. Moon and P. J. Yoo, *J. Alloys Compd.*, 2024, **999**, 175016.
83 M. Qin, L. Zhang and H. Wu, *Adv. Sci.*, 2022, **9**, 2105553.
84 H. K. Choudhary, R. Kumar, S. P. Pawar, S. Bose and B. Sahoo, *J. Electron. Mater.*, 2020, **49**, 1618–1629.
85 H. A. Alburaih, M. A. ul Haq, A. Jabbar, A. ur Rehman, A. Laref, M. M. Saad Hasb Elkhalig and N. A. Noor, *Magnetochemistry*, 2024, **10**(7), 48.
86 C. Pahwa, S. B. Narang and P. Sharma, *J. Alloys Compd.*, 2020, **815**, 152391.
87 S. P. Sahare, A. V. Wankhade and S. P. Zodape, *Appl. Phys.*, 2023, **129**, 43.
88 M. B. Shelar and S. M. Patange, *Mater. Today Proc.*, 2022, **59**, 1196–1201.
89 A. ur Rehman, S. F. Shaukat, A. S. Haidyrah, M. N. Akhtar and M. Ahmad, *J. Electroceram.*, 2021, **46**, 93–106.
90 R. Qindeel, N. H. Alonizan and L. G. Bousiakou, *J. Mater. Sci.: Mater. Electron.*, 2020, **31**, 19672–19679.
91 H. M. T. Farid, I. Ahmad, I. Ali, S. M. Ramay, A. Mahmood and G. Murtaza, *J. Magn. Magn. Mater.*, 2017, **434**, 143–150.
92 S. Gupta, C. Chang, C. H. Lai and N. H. Tai, *Composites, Part B*, 2019, **164**, 447–457.
93 Q. Lu, K. Choi, J.-D. Nam and H. J. Choi, *Polymers*, 2021, **13**, 512.
94 Y. Zhang, Z. Leng, Z. Dong, Z. Liu, Z. Zhang and Z. Tan, *Constr. Build. Mater.*, 2018, **158**, 855–863.